

NRC Publications Archive Archives des publications du CNRC

Investigations of water droplet impact and freezing on a cold substrate with the Lattice Boltzmann method

García Pérez, Jesús; Leclaire, Sébastien; Ammar, Sami; Trépanier, Jean-Yves; Reggio, Marcelo; Benmeddour, Ali

This publication could be one of several versions: author's original, accepted manuscript or the publisher's version. / La version de cette publication peut être l'une des suivantes : la version prépublication de l'auteur, la version acceptée du manuscrit ou la version de l'éditeur.

For the publisher's version, please access the DOI link below. / Pour consulter la version de l'éditeur, utilisez le lien DOI ci-dessous.

Publisher's version / Version de l'éditeur:

<https://doi.org/10.1016/j.ijft.2021.100109>

International Journal of Thermofluids, 12, C, 2021-09-02

NRC Publications Archive Record / Notice des Archives des publications du CNRC :

<https://nrc-publications.canada.ca/eng/view/object/?id=462e8a6b-8bab-4f0c-9974-caeed7dddf25>

<https://publications-cnrc.canada.ca/fra/voir/objet/?id=462e8a6b-8bab-4f0c-9974-caeed7dddf25>

Access and use of this website and the material on it are subject to the Terms and Conditions set forth at

<https://nrc-publications.canada.ca/eng/copyright>

READ THESE TERMS AND CONDITIONS CAREFULLY BEFORE USING THIS WEBSITE.

L'accès à ce site Web et l'utilisation de son contenu sont assujettis aux conditions présentées dans le site

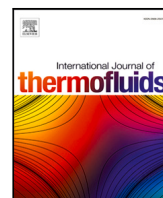
<https://publications-cnrc.canada.ca/fra/droits>

LISEZ CES CONDITIONS ATTENTIVEMENT AVANT D'UTILISER CE SITE WEB.

Questions? Contact the NRC Publications Archive team at

PublicationsArchive-ArchivesPublications@nrc-cnrc.gc.ca. If you wish to email the authors directly, please see the first page of the publication for their contact information.

Vous avez des questions? Nous pouvons vous aider. Pour communiquer directement avec un auteur, consultez la première page de la revue dans laquelle son article a été publié afin de trouver ses coordonnées. Si vous n'arrivez pas à les repérer, communiquez avec nous à PublicationsArchive-ArchivesPublications@nrc-cnrc.gc.ca.



Investigations of water droplet impact and freezing on a cold substrate with the Lattice Boltzmann method

Jesús García Pérez^{a,*}, Sébastien Leclaire^a, Sami Ammar^a, Jean-Yves Trépanier^a, Marcelo Reggio^a, Ali Benmeddour^b

^a Department of Mechanical Engineering, Polytechnique Montreal, Montreal, Quebec, H3T 1J4, Canada

^b National Research Council of Canada, 1200 Montreal Road, Ottawa, ON, K1A 0R6, Canada

ARTICLE INFO

Keywords:

Lattice Boltzmann method
Pseudo-potential
Contact angle
Phase change
Droplet

ABSTRACT

A multiphase Lattice Boltzmann model with phase change is presented for studying droplet impact and solidification on an airfoil. The proposed model combines a pseudo-potential multiphase model and a thermal single-component phase change model. These two models are verified separately. The pseudo-potential model with the Peng–Robinson equation of state is used to simulate large density ratios of multiphase flows. The thermal model is based on the total enthalpy and allows the phase change without using an iterative methodology. The coupling is made through the immersed moving boundary method that handles the solid–liquid interface. The generalization for curved surfaces is introduced through to a novel extrapolation method at boundaries. The effects of surface wettability, static contact angle and initial velocity of the droplet on the evolution of solid fraction and total freezing time are discussed and compared to other simulation and experimental works.

1. Introduction

Ice build-up on airframe surfaces and rotor/propeller blades presents a major hazard to safe and efficient operations of unmanned aerial vehicles (UAVs) in cold and humid environments. To mitigate icing risk for UAVs, new ice protection systems (IPS) are required as conventional IPS developed for manned aircraft are not suitable for UAVs. One such an IPS solution that is being considered is an icephobic coating, i.e., a coating with low affinity for ice. The definition of new materials with high icephobic properties is an extremely dynamic region of exploration. Most of the research that has been carried out to study the effects of different icephobic surfaces on the freezing process of the water droplets, after they impact on a cold wall, has been experimental [1,2]. Detailed impact and freezing phenomenon of a droplet after its impact on the wall are difficult to observe experimentally because of the limitations of experimental methods and measurement techniques. Physics-based computational modeling and simulation, however, can provide more detailed information that cannot be obtained experimentally. If successful, it will allow a better understanding of the impact and freezing phenomenon of water droplets on different icephobic coatings which will result in a better assessment and evaluation of these coatings, for ice protection of UAVs. Numerical simulations assessing the anti-icing systems could be

performed as in [3] for the comparison with experimental studies for a glass fiber reinforced aluminum ice protection system.

The simulation of a water droplet impact and freezing can be modeled with a multi-phase model that accounts for the presence of a liquid phase in a gas and allows interaction with the surface. On the other hand, it is intended to model the transient heat transfer during phase changes, for which a thermal model is required. The numerical simulation of multiphase flows with phase change has appeared in recent years as a challenge because of the inherent difficulty of tracking the various fluid interfaces. Inroads have been made in the simulation of three-dimensional multiphase flows using front capturing methods, like the Volume of Fluid (VOF) [4], the level-set methods [5]. Otherwise, Computational Fluid Dynamic (CFD) solvers can be applied to simulate two-phase flows as in Rosettani et al. [6] for the pumping of a gas–liquid metal. However, the difficulty of maintaining the interface connectivity remains. Some recent publications using these methods have performed the water droplet impact and freezing [7–9]. Alternatively, the lattice Boltzmann method (LBM) has recently achieved success in some areas in which traditional methods show difficulty performing the simulation of multiphase and multicomponent flows in complex geometry. There are several LBM models proposed to solve multiphase flows: the color gradient model [10], the Shan–Chen (SC) pseudo-potential model [11], the phase-field model [12] and

* Corresponding author.

E-mail address: jesus.garcia-perez@isae-superaero.fr (J. García Pérez).

<https://doi.org/10.1016/j.ijtf.2021.100109>

Received 6 April 2021; Received in revised form 9 July 2021; Accepted 27 July 2021

Available online 23 August 2021

2666-2027/© 2021 The Authors.

Published by Elsevier Ltd.

This is an open access article under the CC BY-NC-ND license

(<http://creativecommons.org/licenses/by-nc-nd/4.0/>).

the free energy model [13] are frequently encountered. The pseudo-potential model is probably the most frequently used, as there is no need to add an equation to track the interface between phases and the interface is not introduced as a boundary condition (BC). Regarding the phase change, the LBM model for phase change has recently attracted great attention as it allows the tracking of the liquid–solid interface automatically in a simple way. Many LBMs for solving the phase change have been proposed. They can be classified into three main methods [14]: the enthalpy-based method [15], the phase-field method [16], and the immersed boundary method [17]. The enthalpy based method established by Jiaung et al. [15] is the pioneering work on phase change using the LBM. It uses the evolution of the enthalpy to solve the temperature field and the phase interface is tracked directly by the enthalpy formation. All these multiphase and phase change LB models have proved that the LBM is a promising alternative over conventional methods and therefore a great tool for simulating multiphase flows and phase change materials. For this reason, several LBM models of a water droplet impacting and/or freezing have been proposed in the literature for the integration of both models. They privileged the Shan–Chen pseudo-potential model to simulate multiphase/multicomponent flows, whereas enthalpy-based models are used for phase change.

Sun et al. [18] developed an LBM with phase change capabilities and applied it to the solidification of a static droplet on a surface. The iterative phase change model of Jiaung [15] was coupled with the basic Shan–Chen model [11]. Comparisons of the numerical model with the experiments that they performed, showed the potential of the approach. However, the iterative phase change model increases the simulation time considerably. Xu et al. [19] proposed a two-dimensional model for the solidification of water droplets on a substrate with the coupling between the multicomponent pseudo-potential model and the novel total enthalpy method for phase change. The interface treatment was made with the immersed boundary method. However, no verification or validation is presented to support the feasibility of their findings. The aforementioned models simulated the solidification of static droplets on cold substrates. For water droplet impacting cold substrates and freezing, a model was proposed by Zhao et al. [20]. They proposed a 2D coupled Jiaung’s iterative phase change model with a multiphase S&C model improved by a real Equation of State (EOS). The interface treatment used was an immersed boundary scheme. Effects of freezing temperatures, impact velocity and wettability on freezing time were investigated. Their results were not compared with any other reference and only a cold spot was considered on the surface. Subsequently, Xiong et al. [21] used a multicomponent pseudo-potential model coupled with Jiaung’s iterative phase change model and the immersed boundary scheme to simulate a 3D droplet impact and freezing on a cold rough plate. The effects of roughness of the substrate on the air entrapment for a droplet impact and solidification were studied.

In this work, we performed a mesoscopic study based on a lattice Boltzmann model to simulate a water droplet static freezing and droplet impact and freezing on curved surfaces. Bi-dimensional and three-dimensional versions of the model were implemented. Effects of surface wettability, as well as droplet size and surface temperatures, were investigated and compared to other simulation and experimental results from the literature. To the knowledge of the authors, no other works have presented the coupled multiphase S&C pseudo-potential model and the total enthalpy method [22]. Unlike the commonly used Jiaung method [15] for the phase change, the novel total enthalpy method avoids iterations at every time step to solve the thermal lattice Boltzmann equation. Comparisons with analytical solutions for Stefan problems in [22] showed the accuracy of the method. Furthermore, the generalization of the model to curved surfaces was achieved through an innovative approach for the treatment of interaction forces at the boundary. An application was carried out on a NACA 0012 airfoil.

2. Numerical method

In this section, we will briefly describe the lattice Boltzmann model used to perform the simulations. A double distribution function model was applied, one for the velocity field of the multiphase flow based on the pseudo-potential model, and the second for the temperature field. The following subsections are organized as follows: first, the multiphase LBM is introduced in Section 2.1, and the thermal model is presented in Section 2.2. Finally, the boundary conditions used are described in Section 2.3.

2.1. Multiphase lattice Boltzmann model

The lattice Boltzmann equation (LBE) for the evolution of velocity with the exact difference method (EDM) [23] and immersed boundary scheme [24] is described as:

$$f_i(\mathbf{x} + \mathbf{e}_i \Delta t, t + \Delta t) = f_i(\mathbf{x}, t) - \frac{1-B}{\tau} [f_i(\mathbf{x}, t) - f_i^{eq}(\mathbf{x}, t)] + B\Omega_i^s + (1-B)\Delta t F_i \quad (1)$$

where f_i is the density distribution function at a node \mathbf{x} and time t . The discrete velocity in direction i is given by \mathbf{e}_i . In this work, we use the D2Q9 (D3Q19 for 3D) lattice. The relaxation time τ is related to the fluid viscosity through $\nu = \Delta t c_s^2 (\tau - 1/2)$, where c_s is the lattice sound speed given by $c_s = c/\sqrt{3}$ with $c = \Delta x/\Delta t$, $\Delta x = \Delta t = 1$, Δx is the lattice spacing and Δt the time step.

The immersed boundary method is introduced by the weighting factor B which relates the dimensionless relaxation time with the fluid liquid fraction f_l :

$$B = \frac{(1-f_l)(\tau-0.5)}{f_l + \tau - 0.5} \quad (2)$$

where f_l is the volume-phase fraction of the liquid phase. For the solid region f_l is equal to zero and is equal to unity for the liquid region. The additional term Ω_i^s represents the collision which bounces back the non-equilibrium part of the distribution function.

$$\Omega_i^s = f_i(\mathbf{x}, t) - f_i(\mathbf{x}, t) + f_i^{eq}(\rho, \mathbf{u}_s) - f_i^{eq}(\rho, \mathbf{u}) \quad (3)$$

where \mathbf{u}_s is the solid velocity (zero for our simulations) and \bar{i} represents the opposite direction of i .

The function at the equilibrium f_i^{eq} is given by :

$$f_i^{eq}(\rho, \mathbf{u}) = \rho \omega_i \left[1 + \frac{\mathbf{e}_i \cdot \mathbf{u}}{c_s^2} + \frac{\mathbf{u} \mathbf{u} : (\mathbf{e}_i \mathbf{e}_i - c_s^2 \mathbf{I})}{2c_s^2} \right] \quad (4)$$

where ω_i is the weight coefficient in the direction i . The force term is introduced by the exact difference method :

$$\Delta t F_i(\mathbf{x}, t) = f_i^{eq}(\rho, \mathbf{u} + \Delta \mathbf{u}) - f_i^{eq}(\rho, \mathbf{u}) \quad (5)$$

where $\Delta \mathbf{u}$ is the velocity difference due to total force given as:

$$\Delta \mathbf{u} = \mathbf{F} \Delta t / \rho \quad (6)$$

The total force $\mathbf{F} = \mathbf{F}_i + \mathbf{F}_s + \mathbf{F}_g$, is made up of three forces: contains the interaction force between phases \mathbf{F}_i , the interaction force between the fluid and solid \mathbf{F}_s , and the gravity force \mathbf{F}_g . The fluid–fluid and solid–fluid interactions are described in Sections 2.1.1 and 2.1.2, respectively. The gravity force can be calculated by using the following expression :

$$\mathbf{F}_g = \mathbf{g}(\rho - \rho_g) \quad (7)$$

which means that the force only affects the liquid phase. Finally, macroscopic properties are calculated by adding up for all the discrete directions :

$$\rho = \sum_i f_i, \quad \mathbf{u} = \sum_i f_i \mathbf{e}_i \quad (8)$$

with EDM, the real fluid velocity \mathbf{v} is calculated by averaging the momentum before and after collision :

$$\rho \mathbf{v} = \rho \mathbf{u} + \frac{\Delta t}{2} \mathbf{F} \quad (9)$$

2.1.1. Fluid–fluid interaction

The inter-particle force interaction is given by :

$$\mathbf{F}_i = -c_0 \varphi(\mathbf{x}) g \nabla \varphi(\mathbf{x}) \quad (10)$$

where c_0 is a constant depending on the lattice structure. The parameter g controls the strength of the interaction force. Its sign determines whether the force is attractive (negative) or repulsive (positive). The gradient calculation is based on the discretization S214 from Leclaire et al. [25].

The effective mass φ is a function of the local density $\varphi(\mathbf{x}) = \varphi(\rho(\mathbf{x}))$ and its choice allows for the simulation of different fluid mixture behaviors. Considering that the ideal EOS of the system $p = \rho c_s^2$ is corrected by the introduction of this interaction force, the following non-ideal EOS is given :

$$p = c_s^2 \rho + \frac{c_0}{2} g [\varphi(\rho)]^2$$

The effective mass can be defined as follows [11] :

$$\varphi(\rho) = \sqrt{\frac{2(p - c_s^2 \rho)}{c_0 g}}$$

The relationship between pressure and density depends on the choice of the EOS. It should be noted that with this definition of the effective mass and unlike the original Shan–Chen model, the coefficient which models the interaction strength g loses influence on the interaction force and the only condition it needs to satisfy is to ensure that the whole term inside the square root is positive. The choice of the EOS will determine the maximum density ratio and the influence of spurious currents. In this work, we will use the Peng–Robinson equation :

$$p = \frac{\rho RT}{1 - b\rho} - \frac{a\alpha(T)\rho^2}{1 + 2b\rho - b^2\rho^2} \quad (11)$$

$$\alpha(T) = [1 + (0.37464 + 1.5422\omega - 0.26992\omega^2)(1 - \sqrt{T/T_c})]^2 \quad (12)$$

with

$$a = \frac{0.45724R^2T_c^2}{p_c}, \quad b = \frac{0.0778RT_c}{p_c}$$

where T is the absolute temperature of the fluid, a is the attraction parameter and b is the repulsion parameter, and they govern the surface tension. The critical temperature and critical pressure are given by T_c and p_c , respectively. The gas constant is R (set to $R = 1$ for all the simulations) and ω is the acentric factor ($\omega = 0.344$ for water) which is a parameter that measures the non-sphericity of the molecules.

2.1.2. Fluid–solid interaction

The fluid–solid interaction force is given by [26] :

$$\mathbf{F}_s = -g_s \varphi(\mathbf{x}) \sum_i s(\mathbf{x} + \mathbf{e}_i) \omega_i \mathbf{e}_i \quad (13)$$

where s is an indicator function which equals 1 for solid nodes and 0 for fluid nodes. The coefficient g_s is modified to achieve different contact angles. Hydrophilic ($<90^\circ$) and hydrophobic ($>90^\circ$) contact angles are obtained by negative and positive values of g_s , respectively.

For the calculation of the gradient of effective mass in Eq. (10) for fluid–fluid interaction at the boundaries, densities of fluid nodes next to the boundary can be copied to the ghost nodes as applied in Khajepour et al. [27]. However, we proposed an alternative based on the paper of Leclaire et al.'s [28] paper for the extrapolation of the density which uses a prediction step for the calculation of the gradient at the boundary nodes. In this work, the effective mass values calculated at the solid nodes S next to the fluid nodes F (as shown in Fig. 1) were extrapolated using the fluid nodes with a lattice link weighted average.

$$\varphi(\mathbf{x}_s) = \sum_i \omega_i^s(\mathbf{x}_s) \varphi(\mathbf{x}_s + \mathbf{e}_i \Delta t) \quad (14)$$

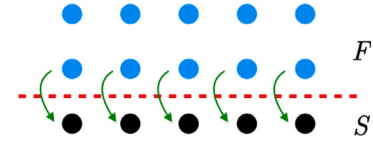


Fig. 1. Schematic of fluid nodes (F) in blue color and solid nodes (S) in black color for the extrapolation from F next to S .

where $\omega_i^s(\mathbf{x}_s)$ is a directional weight calculated depending on the lattice connections between fluid and solid nodes. It is expressed as follows :

$$\omega_i^s = \begin{cases} \frac{\omega_i}{\omega_{\text{total}}^s(\mathbf{x}_s)} & \mathbf{x}_s + \mathbf{e}_i \Delta t \in F \\ 0 & \text{otherwise} \end{cases} \quad (15)$$

$$\omega_{\text{total}}^s(\mathbf{x}_s) = \sum_{(i: \mathbf{x}_s + \mathbf{e}_i \Delta t) \in F} \omega_i \quad (16)$$

The novelty of this extrapolation method is that it allows for the generalization of the solid–fluid interaction for any surface, flat or curved. A somewhat similar approach has also been proposed recently in a paper by Coelho et al. [29]. They applied it, instead, to the density field in a pseudopotential multicomponent model. The stability and accuracy of this approach is shown in their works.

2.2. Liquid–solid phase change lattice Boltzmann model

For the phase-change model, we adopted the total enthalpy method proposed by Huang [22]. The evolution of the function distribution for the total enthalpy is the LBE:

$$g_i(\mathbf{x} + \mathbf{e}_i \Delta t, t + \Delta t) = g_i(\mathbf{x}, t) - \frac{1}{\tau_T} [g_i(\mathbf{x}, t) - g_i^{eq}(\mathbf{x}, t)] \quad (17)$$

The relaxation time τ_T is defined as :

$$\frac{\lambda}{\rho C_{p,\text{ref}}} = c_s^2 (\tau_T - 0.5) \Delta t \quad (18)$$

where the reference specific heat $C_{p,\text{ref}}$ is the harmonic mean between the specific heat capacity of liquid $C_{p,l}$ and solid $C_{p,s}$, defined as :

$$C_{p,\text{ref}} = \frac{2C_{p,s}C_{p,l}}{C_{p,s} + C_{p,l}} \quad (19)$$

Considering a two-dimensional representation with a typical D2Q9 (D3Q19 for 3D) lattice, the equilibrium distribution function can be introduced as :

$$f_i = \begin{cases} H - C_{p,\text{ref}}T + \omega_i C_p T \left(\frac{C_{p,\text{ref}}}{C_p} - \frac{\mathbf{I} : \mathbf{u}\mathbf{u}}{2c_s^2} \right), & i = 0 \\ \omega_i C_p T \left[\frac{C_{p,\text{ref}}}{C_p} + \frac{\mathbf{e}_i \cdot \mathbf{u}}{c_s^2} + \frac{(\mathbf{e}_i \mathbf{e}_i - c_s^2 \mathbf{I}) : \mathbf{u}\mathbf{u}}{2c_s^4} \right], & i \neq 0 \end{cases} \quad (20)$$

Total enthalpy, defined as the sum of the sensible enthalpy $C_p T$ and the latent enthalpy $f_i h_{sl}$ (where h_{sl} is the latent heat), is then calculated as :

$$H = \sum_{i=0}^8 g_i \quad (21)$$

The application of thermodynamic relations to this enthalpy is used to calculate the liquid fraction and temperature :

$$f_l = \begin{cases} 0, & H \leq H_s \\ \frac{H - H_s}{H_l - H_s}, & H_s \leq H \leq H_l \\ 1, & H \geq H_l \end{cases} \quad (22)$$

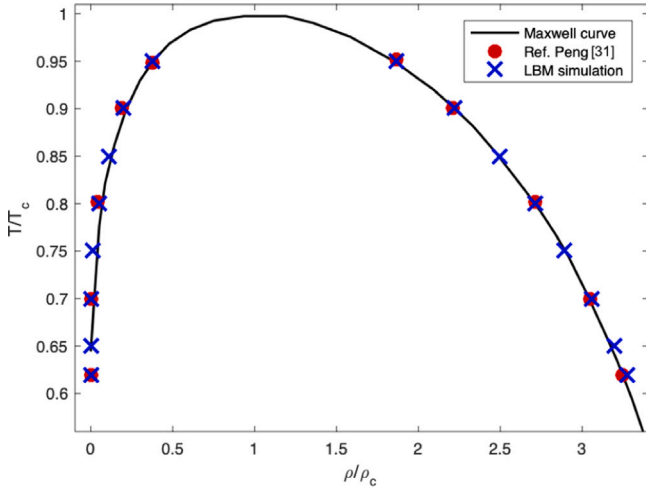


Fig. 2. Coexistence density curve for P-R EOS, Ref. Peng [30].

$$T = \begin{cases} T_s - \frac{H_s - H}{C_{p,s}}, & H \leq H_s \\ \frac{H_l - H}{H_l - H_s} T_s + \frac{H - H_s}{H_l - H_s} T_l, & H_s \leq H \leq H_l \\ T_l + \frac{H - H_l}{C_{p,l}}, & H \geq H_l \end{cases} \quad (23)$$

with $H_s = C_{p,s}T_s$ the total enthalpy at the solid temperature, $H_l = C_{p,l}T_l + h_{sl}$ the total enthalpy at the liquidus temperature T_l . Phase change is considered as happening at a constant temperature, so $T_s = T_l = T_m$, with T_m being the melting or freezing temperature. Thermophysical properties can be expressed in function of the liquid fraction for the entire space as follows :

$$\begin{aligned} \lambda &= (1 - f_l)\lambda_s + f_l\lambda_l \\ C_p &= (1 - f_l)C_{p,s} + f_lC_{p,l} \end{aligned} \quad (24)$$

It should be pointed out that the method presented does not need multiple iterations at every time step to solve the thermal LBE as the latent heat source term was combined with the transient term in the energy equation, which eliminates the source term in the lattice Boltzmann equation so that it is no longer implicit, as it happens in the method of Jiaung et al. [15].

2.3. Boundary conditions

In LBM, the evolution of the fluid is determined by the distribution functions. For this reason, the application of the hydrodynamics quantities on boundaries needs a translation of these macroscopic values to particle distribution functions (PDF). These discrete distribution functions have to be taken care of to reflect the macroscopic BCs of the fluid as they are critical to the stability and accuracy of any numerical solution. For the density function distribution, we used periodic and full-way bounce-back boundary conditions [31]. Bounce-back boundary conditions are typically used to implement no-slip conditions on the boundary. For the thermal distribution function, periodic and Dirichlet boundary conditions were used. The Dirichlet BC are based on Liu et al. [32]. Details and configuration for boundary conditions are specified and explained for each test case.

3. Model verification

As the proposed model is the combination of the multiphase model and the thermal phase change model, we verified both models separately. The multiphase model was verified for all the modules of

forces applied. The application of the equation of state and the fluid–fluid interaction were verified with the phase separation and Laplace’s law. After, the liquid–solid interaction was verified for the contact angles. Meanwhile we verified the phase change model with the Stefan problem for the solidification of a semi-infinite square.

3.1. Pseudo-potential model verification

The following subsections present the verification of the thermodynamic consistency (Section 3.1.1) and the validation of Laplace’s law (Section 3.1.2).

3.1.1. Verification of the thermodynamic consistency

In order to verify the thermodynamic consistency of the multiphase model with the P-R EOS, the phase separation test was simulated. This test case aimed to simulate the phase separation of a fluid from critical density. All the domain was initialized at zero velocity and density was set to its critical value with a slightly random perturbation of 1%. The critical density can be obtained by the EOS after getting the critical temperature and pressure defined by the constants a , b , and R . For P-R, these values were set to $a = 2/49$, $b = 2/21$ and $R = 1$. The temperature was fixed to a value under the critical temperature, thus the interaction force makes the phase separation automatically when the flow becomes steady. The analytical solution to this problem is given by the Maxwell construction that is obtained by the method of equal area [33]. For this purpose, a 100×100 lattice arrangement was chosen to be the computational domain. The force was introduced by using the exact difference method and the relaxation time was set to $\tau = 1$. Results obtained for the coexistence density curve for P-R are presented in Fig. 2, along with the simulation results from [30] with the same EOS and model implemented.

The results show an excellent agreement with the simulations performed by Peng et al. [30], which allow us to verify the implemented model. Regarding the results and their comparison with the Maxwell construction [33], it is inferred that both P-R EOS perform well and agree with the analytical solution.

3.1.2. Verification of Laplace’s law

The surface tension for the multiphase model can be verified through Laplace’s law. The Laplace’s law determines the relationship between the pressure difference and the inverse of the radius of a water droplet or bubble. For a 2D droplet/bubble, the pressure difference between the inside and the outside pressure is given by

$$\Delta P = \frac{\sigma}{r} \quad (25)$$

where σ represents the surface tension and r the radius. For this test, a 100×100 lattice structure was chosen. P-R EOS was used to plot the differences in pressure between the inside and the outside of the water droplet while the radius increases from 14 to 24 lattice units. Periodic conditions were applied in all boundaries and water droplets were initialized by using a tanh function to create a diffusive layer as shown in Eq. (26). The pressure difference was calculated as the difference between the steady-state high pressure inside the droplet and the steady-state low pressure outside the droplet. This pressure difference was plotted against the inverse initial radius for three different reduced temperatures of T/T_c . The values to initialize the density field were determined by the coexistence density curve that was obtained with the phase separation test at each reduced temperature. Periodic conditions were applied at all boundaries. The results presented in Fig. 3 show a linear trend, as expected.

$$\rho(x, y) = \frac{\rho_g + \rho_l}{2} - \frac{\rho_l - \rho_g}{2} \left[\tanh \left(\frac{2\sqrt{(x - x_0)^2 + (y - y_0)^2} - r_0}{W} \right) \right] \quad (26)$$

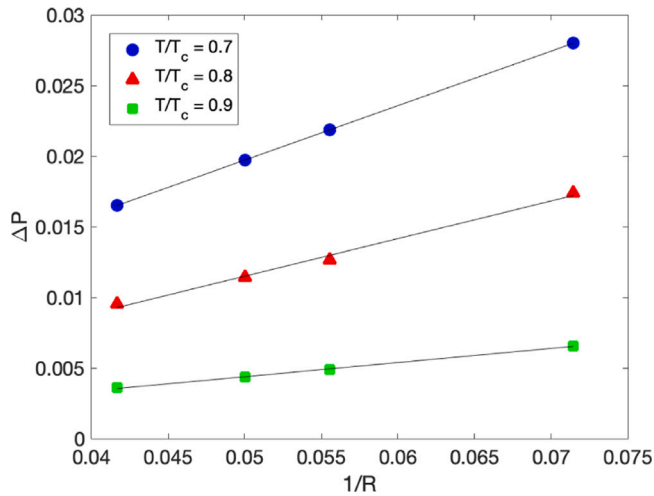


Fig. 3. Pressure difference across droplet vs. inverse radius (in lattice units) simulated at different temperatures for P-R EOS.

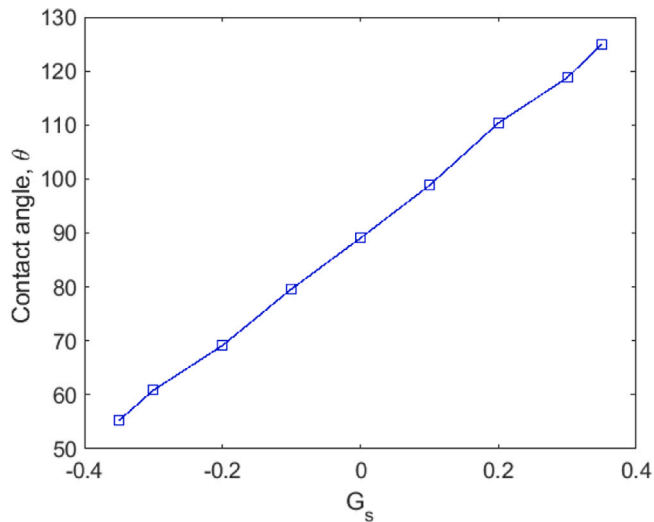


Fig. 4. Contact angle against interaction strength.

3.1.3. Verification of the solid–fluid interaction

The previous two tests allowed us to verify Section 2.1.1 for the pseudo-potential model. In order to verify the solid–fluid interaction from Section 2.1.2, we simulated different contact angles of a water droplet on a wall. For the pseudo-potential model, the relationship between the interaction force coefficient and the contact angle, shown in Fig. 4, was linear in our simulations as observed in previous literature [34]. Besides, for $g_s = 0$, the contact angle obtained was $\theta = 90^\circ$. This allowed us to verify the implementation of the fluid–solid interaction and the treatment of the extrapolation at the boundary.

3.2. Phase change model verification

The total enthalpy model for phase change was validated by simulating a solidification dominated by conduction from a corner in a quarter-space. The liquid started at a uniform temperature T_i higher than the freezing temperature T_f . At $t = 0$, the temperature of the south and left walls were lowered to a constant value T_w below the freezing temperature. Adiabatic boundary conditions were applied at top and right boundaries. The domain is considered to be infinite in both directions. In order to do that with a finite length L , we considered a large number of lattices in both direction and we ensured that at the

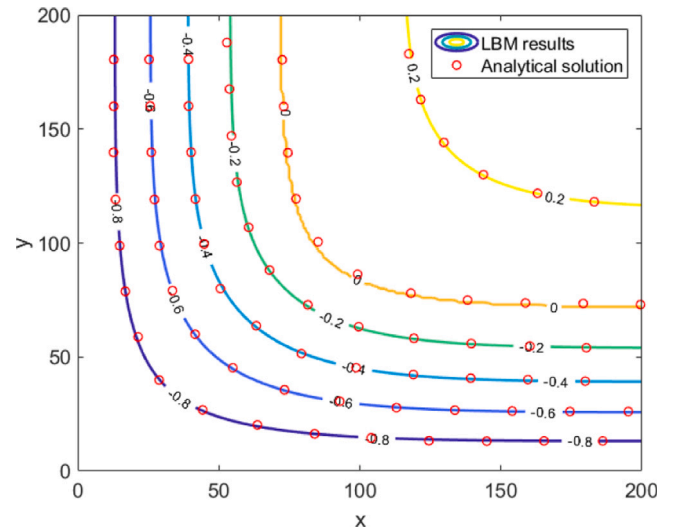


Fig. 5. Comparisons between analytical solution and LB model for the position of the isotherms $T^* = 0.2, 0, -0.2, -0.4, -0.6$, and -0.8 at $t^* = 0.25$.

evaluation time step, the temperature at the right and top walls were fixed at T_w and with a zero slope as adiabatic boundary condition was applied.

The initial temperature was $T_i = 0.3$, while constant temperature boundaries were set to $T_w = -1$. The freezing temperature value is between T_i and T_w and was fixed to $T_f = 0$. The other parameters were as follows: $C_{p,l} = C_{p,s} = 1$, $\lambda_l = \lambda_s = 1$, Stefan number $Ste_v = Ste_s = C_{p,l}(T_m - T_w)/h_{sl} = 4$. Comparisons with the analytical solution provided in [35] for the phase interface position and isotherm lines are presented in Fig. 5 at $t^* = 0.25$. Results show a good agreement with the analytical solution which verifies the ability of the presented method to simulate phase change in two-dimensional cases.

4. Results

Once the models were verified, we could merge the multiphase and phase change models to simulate the impact and freezing of water droplets on cold surfaces. Then, in order to validate the coupling, we have carried out numerical simulations for droplet impact and freezing under different conditions using different geometries. We compare our results with other simulation and experimental results from the literature. Firstly, we will performed the solidification of a static droplet on a cold flat plate. Our three-dimensional implementation was used to compare our results with experimental data found in the literature. Secondly, we performed the impact and freezing of water droplets on a cold flat surface. The influence of the Reynolds number was analyzed. Finally, we exploited the adaptability of the model for curved surfaces by simulating the impact and freezing on a NACA0012 airfoil.

4.1. Droplet solidification on a cold flat plate

The first test concerned the solidification of a droplet on a cold flat plate. In the initial state, the droplet was in a liquid state at the center of the domain and there was no solid phase region. The temperature of the domain was higher than that of the cold flat plate and freezing point. For the velocity field, non-slip boundary conditions were applied on the top and bottom walls. Periodic boundary conditions were used between the left and right sides. For the temperature, periodic boundary conditions are also applied along the sides. Dirichlet boundary conditions were enforced at the bottom cold wall and for the warm temperature on the top.

For this test, we initialized the fluid domain and let the droplet impact the surface under isothermal conditions. There was an initial

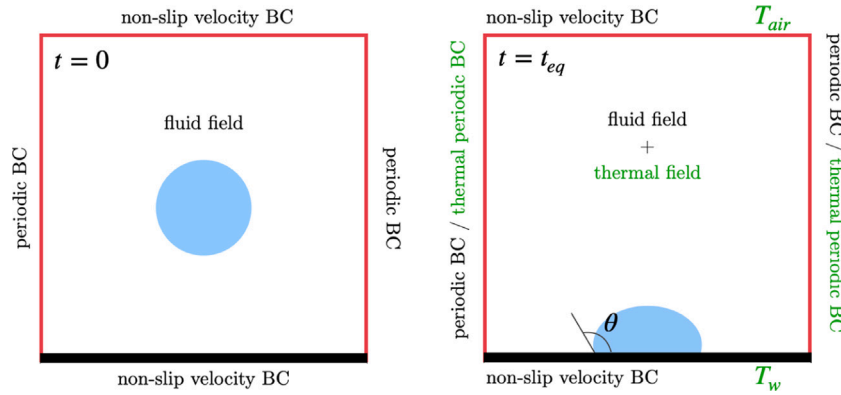


Fig. 6. Boundary conditions and initial state for the isothermal falling droplet (left) and for the temperature field activation at time $t = t_{eq}$ (right).

stage where a droplet deformation period is observed before it finally reached an equilibrium position due to the balance of surface tension, viscous forces, and gravity. Once there was no more deformation on the droplet (a determined simulation time t_{eq} depending on mesh and Reynolds number Re), the thermal field was activated and solidification of the liquid phase started. The boundary conditions and the computational domain for the initial configuration and the thermal boundaries are shown in Fig. 6. Initial conditions for the fluid field with the aforementioned boundary conditions are shown in the left of Fig. 6. When the droplet reached an equilibrium contact angle at t_{eq} , the thermal equation was activated and Dirichlet BC shown in the right of Fig. 6, were applied. The temperature at the surface was lower than the freezing temperature $T_w < T_f$ and the temperature on the top boundary was higher than the freezing temperature $T_{air} > T_f$. This temperature would be the initial temperature of all the domain except for the cold surface. Simulation results are presented in terms of dimensionless numbers. The initial diameter of the droplet D was chosen to be the characteristic length. The dimensionless time and velocity were embedded in the Fourier and Reynolds numbers respectively, while the Stefan number controls the speed of solidification. These dimensionless numbers are defined as:

$$Re = \frac{uD}{\nu}, \quad Fo = \frac{\alpha t}{D^2}, \quad Ste = \frac{C_p(T_f - T_w)}{L_{ls}} \quad (27)$$

where u is the impact velocity (velocity of the droplet just before the contact with the surface is made), ν is the kinematic viscosity, α is the thermal diffusivity, C_p is the liquid heat capacity, T_f is the freezing temperature, T_w the wall temperature and L_{ls} is the latent heat of phase change.

4.1.1. Three-dimensional model for static droplet solidification on a cold plate

The simulation results of this test are compared with experimental results from the literature. For that, a 3D implementation of the model is used.

The computational domain was a grid of $100 \times 100 \times 100$ in lattice units (lu). The droplet had a radius of 16 lu with a center initially at $x = 49.5$, $y = 49.5$ and $z = 25.5$. For the simulations, we choose a reduced temperature of $T_r = 0.8$ which gave a density ratio of approximately 85 between phases. This density ratio was used for all the simulations of this work. The freezing temperature was set to $T_f = 0$ and the wall temperature to $T_w = -2$. The initial temperature was the same as the fixed temperature on top, which was set to $T_i = T_{air} = 0.3$. For thermal properties of fluid and solid, $C_{p,l} = 1$, $\lambda_l = 1/6$, $R_{C_p} = C_{p,s}/C_{p,l} = 0.5$ and $R_\lambda = \lambda_s/\lambda_l = 1$. The Stefan number was set to $Ste = 2$ and the thermal equation was activated at $t_{eq} = 4000$ time steps, when the oscillation of the droplet was finished.

Fig. 7 shows a comparison of the water droplet evolution between our simulation results and photographs from the experimental results

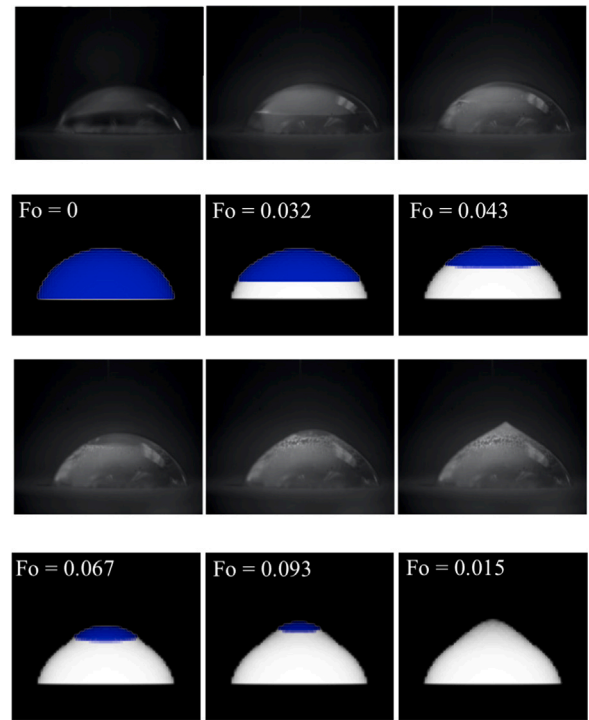


Fig. 7. Comparisons of water droplet evolution on a cold flat plate between simulations and snapshots of the time-sequential images reproduced from HaiFeng Zhang, Yugang Zhao, Rong Lv, Chun Yang. Freezing of sessile water droplet for various contact angles. Source: International Journal of Thermal Sciences; 101 (2016) 59–67 [36]. © 2021 Elsevier Masson SAS. All rights reserved.

of [36]. We represented the same contact angle of $\theta = 79^\circ$ and a qualitative comparison of the evolution of the solidification front is shown. In the simulation results, white and blue colors represent the solid and liquid phases, respectively. We can observe how the concave interface is well displayed in the simulation results and also the volume expansion of the droplet as a result of the density ratio between the liquid and the solid. This effect is more noticeable at the final stage where the top of the droplet deforms and a singular tip appears. As observed in Zhang et al. [36], the volume expansion is slight in the early stage. The tip deformation observed in the experiment is sharper than the one found in the simulation.

The same configuration was used to analyze the temperature field of the domain and determine if it agreed with qualitative expectations. Fig. 8 shows the snapshots of the temperature field for four different time steps 8(a) and the evolution of the temperature along the z -axis above the center of the cold surface at the same time steps 8(b). These

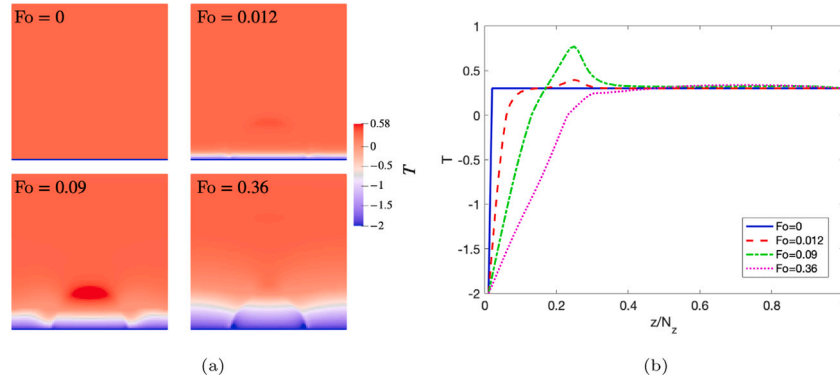


Fig. 8. Snapshots of the temperature field (a) and temperature along the z -axis above the center of the cold plate (b) for four different Fourier numbers.

time steps represent the initial configuration, the start of the freezing, some intermediate point, and the end of the freezing. We can observe how the conduction of the temperature is modified by the presence of the droplet and its freezing. For $Fo = 0.09$ in Fig. 8(b), we can see a slight change of the slope at the liquid–solid interface (at the freezing temperature $T_f = 0$) due to the change of thermal conductivity. Following this, there was a remarkable increase in the temperature because of the liberation of the latent heat. Finally, the temperature reached the ambient constant value. The same trend was observed by Zhao et al. [20] in their LB model for the solidification of water droplets.

4.1.2. Effects of surface wettability on a two-dimensional model

We will now study the influence of contact angle on the solidification process to compare our simulation results with other references. For that, a 2D implementation was used to reduce simulation time and increase the number of nodes used in the domain for a refined grid. Additional tests have been performed showing that the 2D simulations display the same behavior than the 3D model regarding the change of simulation values.

The computational domain was a space of 200×200 in lattice units. The droplet had a radius of 22 lu with the center at $x = 99.5$ and $y = 25.5$. The same droplet density ratio of the 3D simulation was used. Regarding the thermodynamic properties, the following parameters $C_{p,l} = 2C_{p,s} = 1$, and $\lambda_s = \lambda_l = 1/6$, were used for thermal capacity and diffusivity, respectively. These parameters remained the same unless specifically indicated otherwise. As for the temperatures, we used: $T_w = -2$ and $T_i = T_{air} = 0.3$. The droplet is at the same temperature as the surrounding air, i.e. T_{air} .

In order to investigate the effects of the contact angle on the static droplet freezing, different contact angle surfaces were simulated ($\theta = 61^\circ$, $\theta = 75^\circ$, $\theta = 90^\circ$, $\theta = 104^\circ$ and $\theta = 119^\circ$) with the same Stefan number of $Ste = 2$. Fig. 9 shows the snapshots of LB simulated results for the different contact angles at three different dimensionless times: before the freezing process starts, at some point in the middle of the process and the final time of droplet freezing for the larger contact angle. The droplet is indicated in navy blue and the formation of ice in light blue. The wall is represented by a black line. It is shown that for the intermediate dimensionless time, the smaller the contact angle, the more advanced the solidification front is. We can observe that when the case of higher contact angle freezes, smaller cases have also finished the process.

Fig. 10 shows the temporal variation of total solid fraction against Fourier number for the same different contact angles. The total solid fraction is defined as the number of nodes in solid phase divided by the total number of ice phase nodes at the end of the simulation as shown in Eq. (28).

$$\text{total solid fraction } (t) = \frac{\sum_i (1 - f_{li}(t))}{\sum_i (1 - f_{li}(t_f))} \quad (28)$$

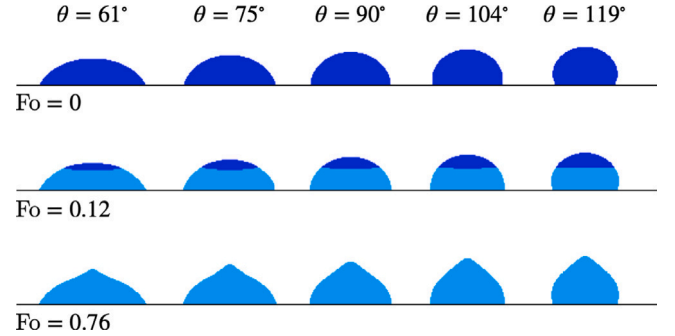


Fig. 9. Snapshots of different contact angles θ of a droplet freezing on a wall at three different dimensionless times Fo .

For its temporal evolution, we can see how the freezing time increased with the contact angle. This was expected because the contact area between the droplet and the cold surface is smaller for larger contact angles, which leads to a less heat released from the droplet and therefore a longer freezing time. So, the surface with a larger contact angle can delay the solidification process. It can be seen that the increasing rate of solid fraction was slower at the final stage than that in the beginning. This was also observed by Sun et al. [18]. Regarding the evolution of the interface, it was observed that the displacement speed of the solid front changed over time and exhibited different trends. There was an accelerated process at the start and the end of the solidification process. This is the result of the large area in contact with the cold substrate at the beginning, and the small volume of the remaining liquid part at the end.

The total dimensionless freezing time ($Fo_f = at_f/D^2$) against the contact angle is illustrated in Fig. 11, which shows that the freezing time increases with the contact angle with a linear trend evolution, as observed in [37] for the range of contact angles simulated. For greater contact angles, the freezing time increased faster.

4.2. Effect of impact velocity on a two-dimensional model

In the previous test case, we studied the freezing of a static droplet over a cold flat plate. We then analyzed the impact and freezing of a droplet over a cold surface. The influences of Reynolds number and contact angle on the freezing time and spreading parameter are studied in this subsection.

To simulate the impact and freezing with the presented model, considering the limitations outlined in Section 4.1, the thermal field was activated once the droplet made contact with the surface. This led to the solidification of the droplet once the contact was made because the surface triggered the nucleation process.

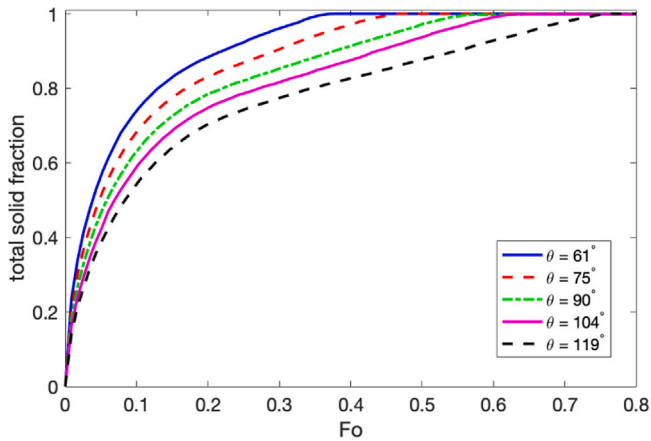


Fig. 10. Effects of contact angle θ on temporal variations of total solid fraction.

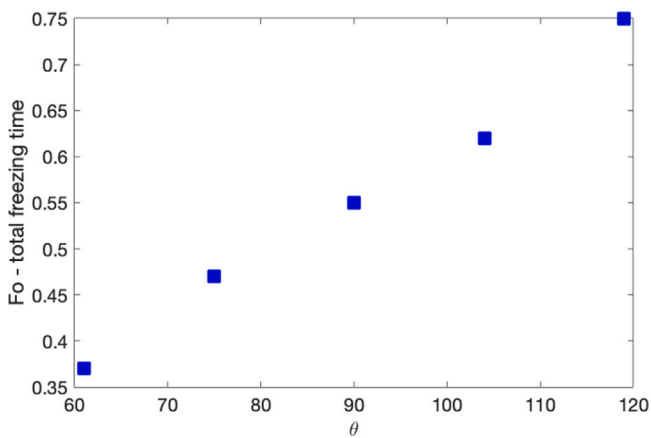


Fig. 11. Variations of total droplet freezing time with different contact angles.

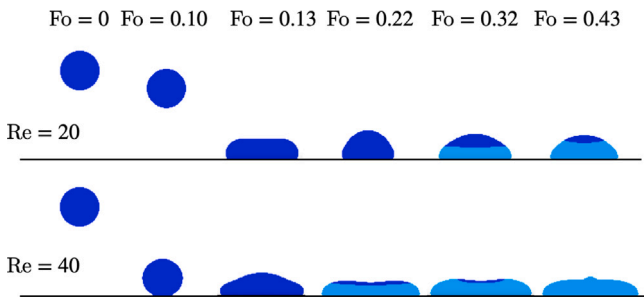


Fig. 12. Snapshots of different Reynolds numbers for the impact and freezing at six time steps.

For this test case, the same previous (Section 4.1.2) two-dimensional grid and thermal parameters were used to carry out the simulations unless otherwise mentioned. The initial diameter of the droplet is set to 22 lu. Regarding the temperatures, we use $T_w = -2$ and $T_{air} = 0.3$.

We analyzed the effects of the Reynolds number based on the impact velocity; we initialized the droplet at the center of the domain ($x = 99.5$, $y = 99.5$) and we change the gravity value in lattice units through the Reynolds number. For this test, we used a hydrophobic surface with a contact angle of $\theta = 119^\circ$ and four Reynolds numbers ($Re = 10$, $Re = 20$, $Re = 30$ and $Re = 40$).

Fig. 12 depicts snapshots of LB simulations for two Reynolds numbers ($Re = 20$ and $Re = 40$) at four different Fourier numbers: initial time, two intermediate instants, and the final freezing for $Re = 40$. We

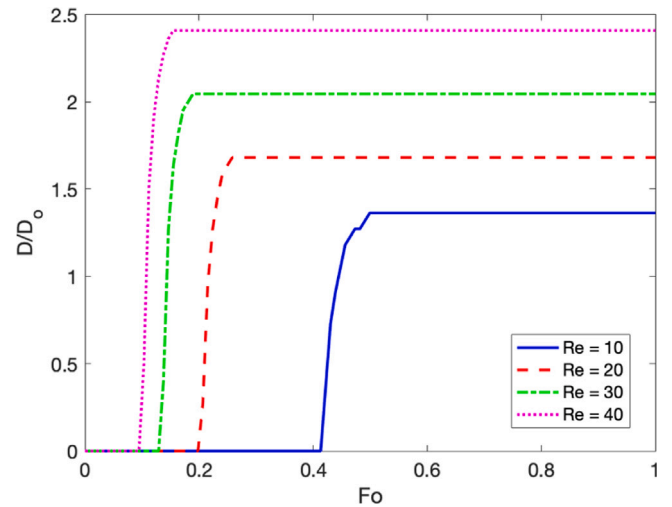


Fig. 13. Temporal variation of spreading factor for different Reynolds numbers.

can observe how a higher Re number resulted in a faster contact of the droplet with the surface and a larger spreading of the droplet on the surface. This faster contact finally produced a rapid complete freezing compared to the lower Re . The freezing time was reduced as Re was increased as a consequence of the augmentation of the contact area of the droplet with the surface. Fig. 13 shows the temporal evolution of the spreading parameter. The spreading parameter is defined as the contact diameter of the droplet on the ice surface divided by the droplet diameter (D/D_0). We can see how the spreading factor increased rapidly up to a maximum value and then remained constant due to the freezing at the contact with the surface. This behavior was also observed by Jin et al. [38] in their experimental results. The instant freezing occurs due to the cold substrate temperature and the increased nucleation rate [39]. This phenomenon appears regardless of the contact angle, as we can observe for a superhydrophobic substrate in [40]. This maximum spreading factor was increased by the Re number because, for higher impact velocities, the deformed diameter was larger for droplets with the same volume. This effect can also be observed in Fig. 12. The larger is the droplet impact velocity, the faster the freezing occurred.

4.3. Droplet impact and solidification on two-dimensional airfoil surfaces

The intended application of this work is the study of the ice accretion on drones. This is mainly caused by the impact and freezing of supercooled large water droplets on the airframe and rotor blades.

As mentioned in the introduction of this section, the proposed model has been coded so that it can perform droplet impact and freezing not only on flat cold surfaces, but also on curved surfaces. This characteristic allowed us to perform the simulation of a water droplet impact and freezing on a NACA0012 airfoil. The scales used for the droplet size and the airfoil agree with what can be found on a drone's rotors. For small drones (under 25 kg) tested in wind tunnels at the National Research Council of Canada, the mean aerodynamic chord of rotor blades is approximately 0.2 cm and during experiments, supercooled large droplets with diameters of approximately 0.4 mm can be found. Such droplet diameter corresponds roughly to 2% of the mean aerodynamic chord of the rotor blades, and close to 20% of the airfoil thickness for NACA0012 profile. Fig. 14 shows snapshots of the simulated water droplet impacting on an airfoil for three different contact angles ($\theta = 61^\circ$ [hydrophilic], $\theta = 90^\circ$ and $\theta = 119^\circ$ [hydrophobic]) at different time steps. We use a 2-dimensional model for the droplet with an initial velocity set to zero. The droplet has an initial diameter of 28 lu. The temperature of the airfoil is set to $T_a = -2$ and the

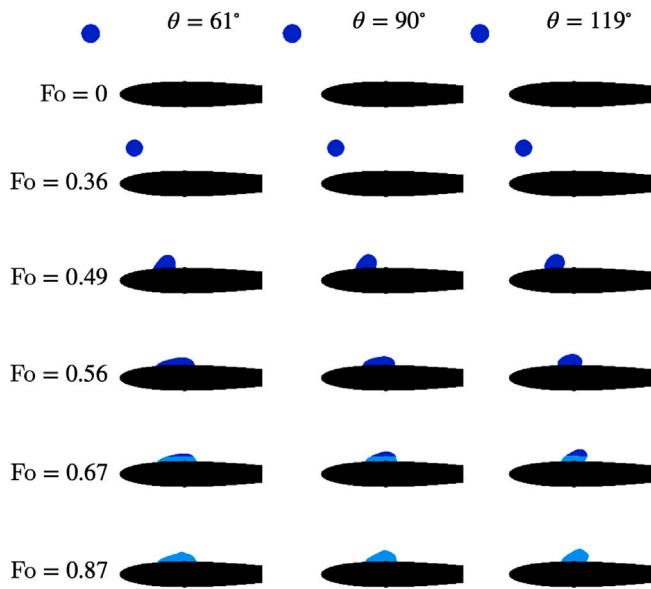


Fig. 14. Snapshots of a water droplet impact and freezing on a NACA0012 airfoil for three different contact angles at different time steps.

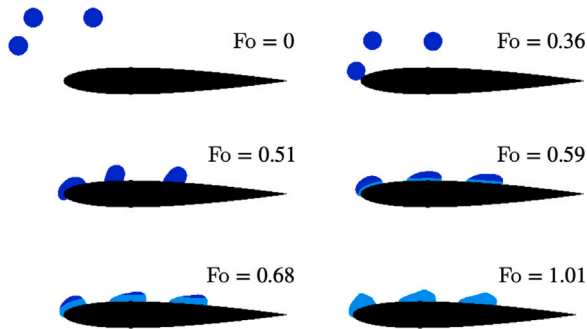


Fig. 15. Snapshots of three water droplets impacting and freezing on a NACA0012 airfoil for $\theta = 90^\circ$ at different time steps.

initial temperature for the droplet and surroundings is $T_{air} = 0.3$. The dimensionless numbers are: $Re = 50$ and $Ste = 2$. We can observe how a smaller contact angle results in a larger contact area with the surface and therefore faster freezing. For the hydrophobic surface, there is a runoff of the droplet before it starts freezing. It should be mentioned here that in our simulation we are not considering steady state flow. This may provide the droplet with another source for leaving the airfoil before freezing starts. This highlights the capability of the hydrophobic surfaces to delay the freezing or even to avoid it.

Finally, we outline the capability of the proposed model to perform the simulation of the impact and freezing of several not colliding droplets at the same time. The simulation results are presented in Fig. 15, where we simulated three droplets impacting a surface with a contact angle of $\theta = 90^\circ$, $Re = 50$ and $Ste = 2$. Snapshots show how droplets adapt to the surface, and the initial spreading determine the nucleation area for the solidification. Deformation of the final frozen form displays the inertia of the droplet and the inclined angle of impinging.

5. Conclusion

In this study, a lattice Boltzmann model for droplets impact and freezing was described and implemented. A double distribution function approach was used to couple the multiphase pseudo-potential

model and the total enthalpy model for phase change. The coupling was made through the application of the Immersed Boundary Scheme.

A qualitative comparison of a three-dimensional model with experimental and simulation results, revealed the potential of the current methodology. It was observed that the concave interface and volume expansion are properly predicted by the simulation. A 2D model was then used to analyze the influence of some parameters on the solidification of a static droplet on a cold flat plate and compared them with simulation results from the literature. The current predictions corroborated that higher contact angles (corresponding to hydrophobic surfaces) delay the freezing, because of the reduced contact area with the surface.

The impact and freezing were performed later. Instant freezing was simulated indicating that higher impact velocities result in a larger contact area, and therefore in a faster freezing. Finally, the potential of the model for handling impinging water on curved surfaces was shown by predicting the impact and freezing of droplets over an airfoil.

The provided methodology analysis and simulation results are quite encouraging for this preliminary research step, aimed to the development of new numerical tools, for ice accretion prediction arising in unmanned aircraft. In the short term, we point to the following improvements to be made :

- A multi-component model with a double distribution function, in order to change the viscosity of the phases.
- A temperature boundary condition at the interface of droplets, to allow the freezing of precipitations impinging on already frozen droplets on a surface.

Declaration of competing interest

The authors declare that they have no known competing financial interests or personal relationships that could have appeared to influence the work reported in this paper.

Acknowledgment

The authors gratefully acknowledge the financial support from the National Research Council of Canada (NRC).

References

- [1] R. Attarzadeh, A. Dolatabadi, Icephobic performance of superhydrophobic coatings: A numerical analysis, *Int. J. Heat Mass Transfer* 136 (2019) 1327–1337, <http://dx.doi.org/10.1016/j.ijheatmasstransfer.2019.03.079>.
- [2] L. Tian, Y. Liu, L. Li, H. Hu, An experimental study to evaluate hydro-/ice-phobic coatings for icing mitigation over rotating aero-engine fan blades, in: *SAE Technical Paper*, SAE International, 2019, <http://dx.doi.org/10.4271/2019-01-1980>.
- [3] M.Z. Hasan, Experimental and numerical analysis of anti-icing a GLARE laminate, *Int. J. Thermo fluids* 10 (2021) 100087, <http://dx.doi.org/10.1016/j.ijft.2021.100087>, URL <https://www.sciencedirect.com/science/article/pii/S2666202721000252>.
- [4] C. Hirt, B. Nichols, Volume of fluid (VOF) method for the dynamics of free boundaries, *J. Comput. Phys.* 39 (1) (1981) 201–225, [http://dx.doi.org/10.1016/0021-9991\(81\)90145-5](http://dx.doi.org/10.1016/0021-9991(81)90145-5).
- [5] J. Sethian, Evolution, implementation, and application of level set and fast marching methods for advancing fronts, *J. Comput. Phys.* 169 (2) (2001) 503–555, <http://dx.doi.org/10.1006/jcph.2000.6657>.
- [6] J. Rosettani, W. Ahmed, P. Geddis, L. Wu, B. Clements, Experimental and numerical investigation of gas-liquid metal two-phase flow pumping, *Int. J. Thermo fluids* 10 (2021) 100092, <http://dx.doi.org/10.1016/j.ijft.2021.100092>, URL <https://www.sciencedirect.com/science/article/pii/S2666202721000306>.
- [7] C. Shinan, D. Liang, S. Mengjie, L. Mengyao, Numerical investigation on impingement dynamics and freezing performance of micrometer-sized water droplet on dry flat surface in supercooled environment, *Int. J. Multiph. Flow.* 118 (2019) 150–164.
- [8] X. Zhang, X. Liu, X. Wu, J. Min, Impacting-freezing dynamics of a supercooled water droplet on a cold surface: Rebound and adhesion, *Int. J. Heat Mass Transfer* 158 (2020) 119997.
- [9] V. Thiévenaz, T. Séon, C. Josserand, Solidification dynamics of an impacted drop, *J. Fluid Mech.* 874 (2019) 756–773, <http://dx.doi.org/10.1017/jfm.2019.459>.

- [10] A.K. Gunstensen, D.H. Rothman, S. Zaleski, G. Zanetti, Lattice Boltzmann model of immiscible fluids, *Phys. Rev. A* 43 (1991) 4320–4327, <http://dx.doi.org/10.1103/PhysRevA.43.4320>.
- [11] X. Shan, H. Chen, Lattice Boltzmann model for simulating flows with multiple phases and components, *Phys. Rev. E* 47 (1993) 1815–1819, <http://dx.doi.org/10.1103/PhysRevE.47.1815>.
- [12] X. He, S. Chen, R. Zhang, A lattice Boltzmann scheme for incompressible multiphase flow and its application in simulation of Rayleigh–Taylor instability, *J. Comput. Phys.* 152 (2) (1999) 642–663, <http://dx.doi.org/10.1006/jcph.1999.6257>.
- [13] M.R. Swift, W.R. Osborn, J.M. Yeomans, Lattice Boltzmann simulation of nonideal fluids, *Phys. Rev. Lett.* 75 (1995) 830–833, <http://dx.doi.org/10.1103/PhysRevLett.75.830>.
- [14] R. Huang, H. Wu, Phase interface effects in the total enthalpy-based lattice Boltzmann model for solid–liquid phase change, *J. Comput. Phys.* 294 (2015) 346–362, <http://dx.doi.org/10.1016/j.jcp.2015.03.064>.
- [15] W.-S. Jiaung, J.-R. Ho, C.-P. Kuo, Lattice Boltzmann method for the heat conduction problem with phase change, *Numer. Heat Transf. B - Fund.* 39 (2001) <http://dx.doi.org/10.1080/10407790150503495>.
- [16] W. Miller, S. Succi, D. Mansutti, Lattice Boltzmann model for anisotropic liquid-solid phase transition, *Phys. Rev. Lett.* 86 (2001) 3578–3581, <http://dx.doi.org/10.1103/PhysRevLett.86.3578>.
- [17] R. Huang, H. Wu, An immersed boundary-thermal lattice Boltzmann method for solid–liquid phase change, *J. Comput. Phys.* 277 (2014) 305–319, <http://dx.doi.org/10.1016/j.jcp.2014.08.020>.
- [18] J. Sun, J. Gong, G. Li, A lattice Boltzmann model for solidification of water droplet on cold flat plate, *Int. J. Refrig.* 59 (2015) 53–64, <http://dx.doi.org/10.1016/j.ijrefrig.2015.07.003>.
- [19] P. Xu, S. Xu, Y. Gao, P. Liu, A multicomponent multiphase enthalpy-based lattice Boltzmann method for droplet solidification on cold surface with different wettability, *Int. J. Heat Mass Transfer* 127 (2018) 136–140, <http://dx.doi.org/10.1016/j.ijheatmasstransfer.2018.07.017>.
- [20] J. Zhao, X. Li, P. Cheng, Lattice Boltzmann simulation of a droplet impact and freezing on cold surfaces, *Int. Commun. Heat Mass Transfer* 87 (2017) <http://dx.doi.org/10.1016/j.icheatmasstransfer.2017.07.006>.
- [21] W. Xiong, P. Cheng, Mesoscale simulation of a molten droplet impacting and solidifying on a cold rough substrate, *Int. Commun. Heat Mass Transfer* 98 (2018) 248–257, <http://dx.doi.org/10.1016/j.icheatmasstransfer.2018.09.001>.
- [22] R. Huang, H. Wu, P. Cheng, A new lattice Boltzmann model for solid–liquid phase change, *Int. J. Heat Mass Transfer* 59 (2013) 295–301, <http://dx.doi.org/10.1016/j.ijheatmasstransfer.2012.12.027>.
- [23] A. Kupershtokh, D. Medvedev, D. Karpov, On equations of state in a lattice Boltzmann method, *Comput. Math. Appl.* 58 (5) (2009) 965–974, <http://dx.doi.org/10.1016/j.camwa.2009.02.024>, Mesoscopic Methods in Engineering and Science.
- [24] D.R. Noble, J.R. Torczynski, A lattice-Boltzmann method for partially saturated computational cells, *Internat. J. Modern Phys. C* 09 (08) (1998) 1189–1201, <http://dx.doi.org/10.1142/S0129183198001084>.
- [25] S. Leclaire, M. El-Hachem, J.-Y. Trépanier, M. Reggio, High order spatial generalization of 2D and 3D isotropic discrete gradient operators with fast evaluation on GPUs, *J. Sci. Comput.* 59 (3) (2014) 545–573, <http://dx.doi.org/10.1007/s10915-013-9772-2>.
- [26] S. Ammar, G. Pernaudoat, J.-Y. Trépanier, A multiphase three-dimensional multi-relaxation time (MRT) lattice Boltzmann model with surface tension adjustment, *J. Comput. Phys.* 343 (2017) 73–91, <http://dx.doi.org/10.1016/j.jcp.2017.04.045>.
- [27] S. Khajepour, J. Cui, M. Dewar, B. Chen, A study of wall boundary conditions in pseudopotential lattice Boltzmann models, *Comput. & Fluids* 193 (2019) 103896, <http://dx.doi.org/10.1016/j.compfluid.2018.05.011>.
- [28] S. Leclaire, K. Abahri, R. Belarbi, R. Bennacer, Modeling of static contact angles with curved boundaries using a multiphase lattice Boltzmann method with variable density and viscosity ratios, *Internat. J. Numer. Methods Fluids* 82 (8) (2016) 451–470, <http://dx.doi.org/10.1002/flid.4226>.
- [29] R. Coelho, C. Moura, M. Telo da Gama, N. Araújo, Wetting boundary conditions for multicomponent pseudopotential lattice Boltzmann, 2020.
- [30] Y. Peng, Y. Fei Mao, B. Wang, B. Xie, Study on C-S and P-R EOS in pseudopotential lattice Boltzmann model for two-phase flows, *Internat. J. Modern Phys. C* 28 (2017) <http://dx.doi.org/10.1142/S0129183117501200>.
- [31] B. Chopard, A. Dupuis, A. Masselot, P. Luthi, Cellular automata and lattice Boltzmann techniques: An approach to model and simulate complex systems, *Adv. Complex Syst.* 05 (02n03) (2002) 103–246, <http://dx.doi.org/10.1142/S0219525902000602>.
- [32] C.-H. Liu, K.-H. Lin, H.-C. Mai, C.-A. Lin, Thermal boundary conditions for thermal lattice Boltzmann simulations, *Comput. Math. Appl.* 59 (7) (2010) 2178–2193, <http://dx.doi.org/10.1016/j.camwa.2009.08.043>, Mesoscopic Methods in Engineering and Science.
- [33] C.W. David, The van der Waals Equation as a cubic, 2015.
- [34] Q. Li, K.H. Luo, Q.J. Kang, Q. Chen, Contact angles in the pseudopotential lattice Boltzmann modeling of wetting, *Phys. Rev. E* 90 (2014) 053301, <http://dx.doi.org/10.1103/PhysRevE.90.053301>.
- [35] D. Li, Z.-X. Tong, Q. Ren, Y.-L. He, W.-Q. Tao, Three-dimensional lattice Boltzmann models for solid–liquid phase change, *Int. J. Heat Mass Transfer* 115 (2017) 1334–1347, <http://dx.doi.org/10.1016/j.ijheatmasstransfer.2017.07.048>.
- [36] H. Zhang, Y. Zhao, R. Lv, C. Yang, Freezing of sessile water droplet for various contact angles, *Int. J. Therm. Sci.* 101 (2016) 59–67, <http://dx.doi.org/10.1016/j.jthermalsci.2015.10.027>.
- [37] C. Zhang, H. Zhang, W. Fang, Y. Zhao, C. Yang, Axisymmetric lattice Boltzmann model for simulating the freezing process of a sessile water droplet with volume change, *Phys. Rev. E* 101 (2020) 023314, <http://dx.doi.org/10.1103/PhysRevE.101.023314>.
- [38] Z. Jin, H. Zhang, Z. Yang, Experimental investigation of the impact and freezing processes of a water droplet on an ice surface, *Int. J. Heat Mass Transfer* 109 (2017) 716–724, <http://dx.doi.org/10.1016/j.ijheatmasstransfer.2017.02.055>.
- [39] M. Mohammadi, M. Tembely, A. Dolatabadi, Supercooled water droplet impacting superhydrophobic surfaces in the presence of cold air flow, *Appl. Sci.* 7 (2017) 130, <http://dx.doi.org/10.3390/app7020130>.
- [40] M. Tembely, R. Attarzadeh, A. Dolatabadi, On the numerical modeling of supercooled micro-droplet impact and freezing on superhydrophobic surfaces, *Int. J. Heat Mass Transfer* 127 (2018) 193–202, <http://dx.doi.org/10.1016/j.ijheatmasstransfer.2018.06.104>.